RSC Advances

PAPER

View Article Online
View Journal | View Issue

Cite this: *RSC Adv.*, 2020, **10**, 27662

Mechanistic pathways for the degradation of SMX drug and floatation of degraded products using F–Pt co-doped TiO_2 photocatalysts

Majid Jahdi, *[a] Shivani B. Mishra, *[a] Edward N. Nxumalo,[a] Sabelo D. Mhlanga[b] and Ajay K. Mishra[a]

Received 6th June 2020
Accepted 6th July 2020

DOI: 10.1039/d0ra05009a

rsc.li/rsc-advances

This work presents smart pathways to enhance the photocatalytic activity of TiO_2 *via* co-doping with fluorine (F) and platinum (Pt) to form F–Pt co-doped TiO_2 photocatalysts and investigates the unique and unusual fluorination of the floated products. Our investigations indicate that the crystalline structure of the photocatalysts was a mixture of anatase and brookite phases and that the nanoparticles of the synthesized nanocomposites had nanometric sizes (4–25 nm). The F–Pt co-doped TiO_2 nano-photocatalysts demonstrated degradation of sulfamethoxazole (SMX) drug of >93% within 90 min under direct solar light and 58% degradation within 360 min under a solar simulator. Thus, co-doping TiO_2 with F and Pt atoms to form F–Pt co-doped TiO_2 nanocomposite is an efficient pathway to achieve high photocatalytic performance escorted with the formation of floating metal-fluoropolymer, unlike pristine TiO_2 which has less photocatalytic degradation and no generation of a floating polymer. Our photocatalytic protocol demonstrates that the degradation of SMX started with redox reactions of oxygen and water absorbed on the surface of the prepared nanocomposites to form superoxide anions ($O_2^{\bullet -}$) and hydroxy radicals ($^{\bullet}OH$) which have oxidation superpower. The resultant products were subsequently fluorinated by fluoride radical ions and floated as metal-fluoropolymer.

1. Introduction

Many pharmaceutical industries and hospitals have been found to discharge pharmaceutical wastes directly into the environment. The presence of pharmaceutical compounds in the aquatic environment and their possible effects on living organisms have emerged as a serious environmental concern.[1] Pharmaceuticals are designed to have a physiological response in humans, plants, and animals and they pose significant risks to the aquatic life due to their natural lipophilic tendency to accumulate in the ecosystem, which might lead to the development of antibiotic-resistant microbial strains.[2] Sulfamethoxazole (SMX) belongs to the sulfonamide group and is a representative antibiotic extensively used in both human and veterinary medicine, and thus frequently detected in water resources.[3] Moreover, SMX might have toxic effects on aquatic organisms because of its antibiotic-resistant nature once released into the aquatic systems, thus it needs to be effectively degraded and/or removed from water resources.[4]

The photocatalytic pathway remains one of the most promising environmental cleaning routes to overcome the problem of water contamination by pharmaceuticals. Titanium dioxide (TiO_2) is known as a key nanotechnology photocatalyst due to its unique properties. However, because of its wide band gap (~3.2 eV), TiO_2 has a poor photocatalytic activity toward diverse water pollutants.[5] By employing TiO_2, only a small portion (less than 5%) of sunlight can be exploited for photocatalytic processes; thus, the photocatalytic response is not enough to initiate chemical reactions that may be efficient for the degradation of pollutants in water.[6] The band gap of TiO_2 does not only strictly depend on its crystalline phase but is also strongly controlled by the morphology of TiO_2 and the presence of anionic and/or cationic impurities in the lattice.[7] The incorporation of noble metals such as Au, Ag, Pd, and Pt into semiconductor nanomaterials has been investigated to induce the response of TiO_2 to the visible light as well as enhance the separation of electron–hole pairs, thereby improving the photocatalytic efficiency.[8,9] The modification of TiO_2 matrix with metal ions as dopants has significant a marked influence on the charge carrier (e^-/h^+) recombination and interfacial electron-transfer rates.[10]

Platinum has so far been recognized as an important catalyst for electrochemical applications such as hydrogen production.[11] It is one of the noble metal used to modify and enforce the photocatalytic activity of TiO_2.[12] Xiong Xu (2016) have studied the synergetic effect of Pt and B on the photocatalytic

[a]*Nanotechnology and Water Sustainability Research Unit, College of Science, Engineering and Technology, University of South Africa, Johannesburg, Florida, 1709, South Africa. E-mail: bhards@unisa.ac.za; majid.jahdi@gmail.com; Tel: +2711 670 9199*

[b]*DST/Mintek Nanotechnology Innovation Centre, Council for Mineral Technology (MINTEK), Private Bag X3015 Randburg, 2125, South Africa*

performance of TiO_2 and their impacts on the photocatalytic degradation of phenolic compounds in water.[13] The local structure of Pt species in TiO_2 nanocrystal and its effect on the photocatalytic reactivity were investigated with various analytical methods.[14] The morphology, pH, particle size, dispersion, and oxidation state of Pt nanoparticles are the main parameters that improve and enhance the photocatalytic activity of TiO_2 and thereby extend its adsorption range to the visible light. The latter parameters have been controlled by a simplistic Pt-doping TiO_2 method.[15]

Doping TiO_2 with a single element (metal or non-metal) does not lead to an efficient shift of the photocatalytic activity to the visible region because one dopant alone might add a single energy level to TiO_2 band gap, either above the valence band (VB) or below the conduction band (CB) and produces a small redshift caused by low absorption of the visible light.[7] Besides that, these energy levels can trap only one type of charge carrier, *i.e.* either electrons or holes.[16] On the other hand, co-doping TiO_2 with two different dopants, mainly the combination of metal and non-metal, produces synergic effects to enhance the visible light absorption efficiency and reduce the recombination processes of the photocatalytic generated charges.[16,17] The fluoride ion (F^-), with its high electronegativity and other properties has attracted great interest as an anatase-brookite TiO_2 control agent.[6] It was reported that F^- ions could influence the photocatalytic reactions by occupying the substituted oxygen sites and then create active sites, oxygen vacancies or Ti^{3+} ions.[18] Czoska *et al.* reported that the incorporation of F^- ions in TiO_2 matrix lead to the formation of Ti^{3+} reduced centers due to the charge compensation between Ti^{4+} and F^-, which localize one electron in the t_{2g} orbitals of the metal without generating oxygen vacancies.[19] The presence of F^- as dopant or as a morphology controlling agent play a significant role on the growth of anatase phase.[20] Moreover, the introduction of F^- into TiO_2 lattice enhances the absorptivity of molecules, increases the temperature of anatase-to-rutile phase transformation, and also enhances the surface acidity of TiO_2.[21,22]

In this present study, a rapid one-step microwave-assisted hydrothermal synthesis method was used to synthesize the F–Pt co-doped TiO_2 nanocomposites in order to achieve similar properties of the conventional hydrothermal method within a short time; thus, get an efficient photocatalyst at an effective cost. The purpose of this work was to investigate the synergistic effects of Pt and F on the photocatalytic performance of TiO_2 photocatalysts. Hence, we investigate TiO_2, F-doped TiO_2, and F–Pt co-doped TiO_2 nanocomposites for the degradation of SMX drug using a solar simulator and direct solar light as light energy source and expose the mechanistic models responsible for the photocatalytic processes involved. The advantage of co-doping TiO_2 with Pt and F resides on the enhancement of the photocatalytic activity of TiO_2 based nanocomposites and the generation of an unusual floating polymer on the treated water.

2. Experimental

2.1 Materials and reagents

Titanium butoxide purum, ≥97.0% (gravimetric) with density of 1 g mL^{-1} was used as TiO_2 source. Chloroplatinic acid hexahydrate bioxtra and trifluoroacetic acid were (ReagentPlus® with 99% purity) were used as platinum and fluorine sources, respectively. Sulfamethoxazole ($C_{10}H_{11}N_3O_3S$), a pharmaceutical secondary standard, was used to investigate the photocatalytic performance of prepared nanocomposites. Acrodisc syringe filters equipped with hydrophilic polypropylene (GHP membrane) and having pore size of 0.45 μm were used for filtering samples during the photocatalytic degradation process. 2-Butanol with purity ≥99.5% (Gravimetric) was used as a solvent.[23] GHP membranes and all chemical reagents were commercial products supplied by Sigma Aldrich (South Africa) and used without any further treatment. Deionized water was prepared using a Direct-Q® (Millipore) Purification System in our laboratory (pH = 7.4 at 14.1 °C).

2.2 Synthesis of doped TiO_2

2.2.1 Pre-hydrothermal assisted microwave synthesis. In a 500 mL glass beaker, different amounts of titanium butoxide ($Ti(OC_4H_9)_4$) (*i.e.* 23, 22.6, 22.4, 22.3 and 21.8 mL corresponding to 100, 90, 89.5, 89 and 87% of TiO_2 in terms molar mass, respectively) were dissolved in 100 mL of 2-butanol to synthesize pristine TiO_2, F-doped TiO_2, F–Pt0.5 co-doped TiO_2, F–Pt1 co-doped TiO_2, and F–Pt3 co-doped TiO_2 nanocomposites and then placed the beakers in an ice bath during the reaction process to slow the hydrolysis of TiO_2 in order to assure an homogenous mixture. Meanwhile, 78, 156, and 468 mg of chloroplatinic acid hexahydrate bioxtra ($H_2PtCl_6 \cdot 6H_2O$), equivalent to 0.5, 1.0, and 3.0% of Pt in terms of molar mass, respectively; was added to the solutions, under magnetic stirring for 15 minutes, to synthesize F–Pt*x* co-doped TiO_2 ($x = 0.5$, 1.0 and 3.0% of Pt) nanocomposites. Approximately 2.4 mL of trifluoroacetic acid (CF_3COOH) equivalent to 10% of fluorine in terms of molar mass, was then added to the mixture while stirring to yield F-doped TiO_2 (F–TiO_2) and F–Pt*x* co-doped TiO_2 (FPt*x*–TiO_2). Subsequently, after 30 minutes of stirring while the mixture kept in an ice bath, 5 mL of deionized water was added dropwise. Finally, the mixture was left to stir overnight at room temperature with an average of 27 °C.

2.2.2 Hydrothermal-assisted microwave synthesis. Undoped TiO_2, F-doped TiO_2 and F–Pt*x* co-doped TiO_2 were synthesised by hydrothermal synthesis *via* a microwave-assisted heating method at 180 °C for 1 h using the MDS-6G microwave. After synthesis, the prepared materials were washed with ethanol which possesses a wide dissolving range of organic impurities. This was followed by washing with deionized water several times to neutralize the pH of the synthesized nanocomposites using an Avanti J-HC High Capacity centrifuge at 17 000 rpm min^{-1} for 1 h. The nanomaterials were then dried in an oven at 100 °C for 8 h, crushed in a mortar, and calcined in a muffle furnace at 400 °C for 4 h.

2.3 Analysis of synthesized nanocomposites

The X-ray diffraction (XRD) patterns were obtained using the Rigaku SmartLab with high-resolution diffractometer. High resolution scanning electron microscopy (HR-SEM) images and energy dispersive spectroscopy (EDS) analysis were performed

on a JEOL-7800F Field Emission Scanning Electron Microscope (FE-SEM) with a cathode-luminescence spectrometer. Prior to FE-SEM analysis, the samples were coated with carbon to increase their conductivity and prevent them from charging. The microstructure of the materials was studied using a JOEL JEM-2100 transmission electron microscope (TEM). By using the Perkin-Elmer Lambda 650 UV/VIS spectrophotometer over a wavelength range of 200 to 800 nm, ultraviolet and visible (UV-Vis) absorbance were measured. Band gaps were calculated using both Kubelka–Munk function and Tauc equation. Kubelka–Munk function $F(R)$ is described in eqn (1):

$$F(R) = \frac{(1-R)^2}{2R} \quad (1)$$

where R is the reflectance of the sample.

The Tauc equation for permitted indirect electronic transition is:

$$(\alpha h\nu)^{1/2} = A(h\nu - E_g) \quad (2)$$

where α is the optical absorption coefficient which can be substituted in the Tauc equation by $F(R)$ obtained from Kubelka–Munk function; $h\nu$ is incident photon energy in eV; A is material dependent absorption constant and E_g is band gap energy of the material.[24,25]

2.4 Energy positions of conduction and valence bands

The energy levels for the valence band (VB) potential E_{VB} and conduction band (CB) potentials E_{CB} of the semiconductors (TiO_2 and TiO_2 based nanocomposites) were calculated is using the following empirical equation:

$$E_{VB} = \chi_{semiconductor} - E_e + 0.5E_g \quad (3)$$

where E_{VB} is the valence band potential, $\chi_{semiconductor}$ is the semiconductor electronegativity, E_e is the energy of free electrons *vs.* hydrogen (4.5 eV), and E_g is the band gap energy of the semiconductor (the band gap energy was calculated using Tauc equation for the permitted indirect transition of TiO_2, F–TiO_2, FPt0.5–TiO_2, FPt1–TiO_2 and FPt3–TiO_2.

E_{CB}, conduction band potential of TiO_2, F–TiO_2, FPt0.5–TiO_2, FPt1–TiO_2 and FPt3–TiO_2 semiconductor can be calculated by:

$$E_{CB} = E_{VB} - E_g \quad (4)$$

The absolute electronegativity of TiO_2 and TiO_2 based nanocomposites were calculated using the following equation:

$$\chi_{semiconductor} = [\chi(A)^a\chi(B)^b\chi(C)^c]^{1/(a+b+c)} \quad (5)$$

where a, b, and c represent the number of atoms which constituting the doped semiconductor (TiO_2).[26] $\chi(A)$, $\chi(B)$ and $\chi(C)$ are the electronegativity of each atom of the doped semiconductor. Indeed, the absolute electronegativity of an atom A approximately as $I_A + E_A$ or, probably better for some purposes, as the following:

$$\chi(A) = \frac{I_A + E_A}{2}$$

I_A and E_A are the ionization energy and electron affinity of each atom from the doped semiconductor, respectively.[27]

2.5 Photocatalytic degradation process of SMX

The photocatalytic degradation of SMX drug was monitored using a Lambda 650 UV/VIS spectrometer under UV-visible irradiation at various times including: −30, 0 (after 30 min in dark), 15, 30, 45, 60, 90, 120, 180, 240, and 360 min. Initially, the photocatalytic degradation of SMX was carried out in a 250 mL glass beaker containing 50 mL of SMX (20 mg L^{-1}) and photocatalyst (50 mg), under the following conditions: photolysis of SMX with UV-visible light in the absence of F–Pt co-doped TiO_2 nanocomposites, SMX solution with the synthesized photocatalyst in dark for 30 min under stirring to establish the adsorption–desorption phenomena (interaction between SMX drug and the surface of F–Pd*x* co-doped TiO_2 nanocomposites), and then exposed the mixture of SMX drug and the photocatalyst to the light using solar simulator and direct sunlight radiations.

SMX degradation percentage is calculated using the following equation:

$$\text{Degradation effieciency } (\%) = \left(\frac{C_0 - C}{C_0}\right) \times 100 = \left(\frac{A_0 - A}{A_0}\right) \times 100$$

A_0 is the initial absorbance at λ_{max} of SMX drug ($\lambda_{max} = 267$ nm) before starting the photocatalytic degradation process which could substitute C_0 (initial concentration of SMX) and A is the absorbance at λ_{max} of SMX drug after each sampling intervals during the photocatalytic degradation process which could substitute C (concentration of SMX after each sampling during the photocatalytic degradation process of SMX drug).[28]

It should be mentioned that there was no adjustment of potential for hydrogen (pH) during this study. However, pH of SMX in deionized water was around pH = 6.5 at $T = 14$ °C which been decreased to pH = 5.8 by adding undoped TiO_2. Moreover, the pH of SMX mixed with TiO_2 based nanocomposites (FPt*x*–TiO_2) was, more acidic than with TiO_2, varying between pH = 5.1 and 5.3 at $T = 17$ °C.

3. Result and discussion

3.1 X-ray diffraction (XRD)

The crystalline phase of the prepared TiO_2, F-doped TiO_2 and F–Pt*x* co-doped TiO_2 nanocomposites with different proportions of Pt were evaluated by XRD (Fig. 1). The XRD patterns of all the synthesized nanocomposites exhibited diffraction peaks at 2θ = 25.32°, 37.87°, 48.05°, 54.03°, 55.01°, 62.75°, 68.91°, 70.20°, 75.14° and 82.80° corresponding to the (101), (103)/(004)/(112), (200), (105), (211), (204), (116), (220), (215) and (224) diffraction planes of anatase TiO_2 (JCPDS, file no. 21-1272).[29] The brookite phase was also found to be present in all the XRD patterns. The characteristic peak of brookite at 2θ = 30.77°, which is not

superposed with any diffraction peaks of anatase phase and/or platinum provided evidence of the presence of brookite TiO_2.[30,31] However, it should be noted that there was no existence of rutile crystalline phase of TiO_2.

On the other hand, the peaks at around $2\theta = 39.78°$, 46.23°, 67.57°, 81.35°, 85.71° assigned to the (111), (200), (220), (311), and (222) diffraction planes respectively were present in all XRD patterns (except where there is no Pt present) of FPt*x*–TiO_2 nanocomposites with different intensities according to the amount of Pt as dopant and are in good agreement with the literature.[32,33] The diffraction planes of anatase phase located at $2\theta = 54.03°$, 55.01°, 68.91° and 70.20° reveal that the incorporation of Pt in TiO_2 matrix increased the crystallinity of TiO_2 as shown in the XRD patterns of FPt*x*–TiO_2 nanocomposites compared to TiO_2 and F–TiO_2 nanomaterials.

3.2 High resolution scanning electron microscopy (HR-SEM)

The FE-SEM images and EDS elemental analysis of synthesized nanocomposites (*i.e.*, TiO_2, F–TiO_2, and FPt*x*–TiO_2) are shown in Fig. 2. The almost spherical shape of the nanocomposites was found to be uniform and similar in all synthesized nanocomposites. Moreover, the morphology of TiO_2 based nanocomposites were kept unchanged after doping TiO_2 and the diameters of the doped and co-doped TiO_2 nanocomposites possessed almost the same average sizes as pure TiO_2. The uniform morphology appears in all images is due to the unchanged cristalline phase of TiO_2 after doping F^- and co-doping with Pt. On the other hand, the elemental composition supplied by EDS analysis of (d) TiO_2, (e) F–TiO_2, and (f) FPt*x*–TiO_2 are shown in Fig. 2; indicating high percentage of titanium (Ti) element compared to oxygen (O) element. This big difference generated huge defects in TiO_2 lattice which increased its photocatalytic activity without any further modifications. The small percentage of F element in (e) and (f) samples might be because of the ionic radius of fluorine and/or its high electronegativity.

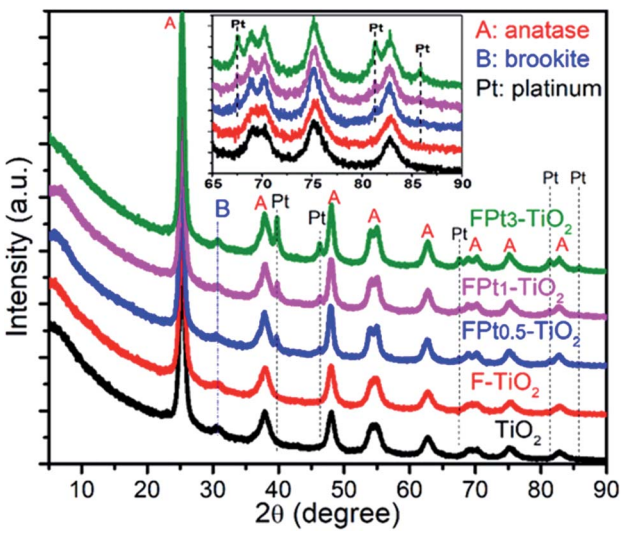

Fig. 1 XRD patterns of TiO_2, F–TiO_2 and FPt*x*–TiO_2 with different proportions of Pt; calcined at 400 °C in air.

3.3 Transmission electron microscopy (TEM)

The morphology and the internal nanostructure of (a) TiO_2, (b) F–TiO_2, and (c) FPt0.5–TiO_2 synthesized nanocomposites were evaluated using TEM. Fig. 3 shows TEM and HRTEM images of (a) TiO_2, (b) F–TiO_2, and (c) FPt0.5–TiO_2 prepared nanocomposites; calcined at 400 °C in air. The nanoparticles of (a) TiO_2, and (b) F–TiO_2 nanomaterials where a mixture of squares and compressed tetragonal shapes with an average diameter range of 10–20 nm as shown in Fig. 3(a) and (b). The HR-TEM images shows that the nanoparticle size of (b) F–TiO_2 nanomaterials was reduced after incorporating fluoride ions (F^-) in the TiO_2 lattice. However, Fig. 3(c) shows a mixture of cubes and compressed tetragonal shapes integrated with dark dots attributed to Pt nanoparticles with an average size of 4–10 nm, forming heterojunction structures.

3.4 UV-Vis absorption, band gap and potential energies positions of TiO_2 based nanocomposite

3.4.1 UV-Vis absorption and band gap. Fig. 4 shows the UV-Vis absorbance in the wavelength range of 250–800 nm and the estimated band gap of TiO_2, F–TiO_2, and FPt*x*–TiO_2 nanocomposites where $x = 0.5$, 1, and 3%. The UV-Vis spectra show (Fig. 4a) an efficient absorption by all nanocomposites samples at UV region, while a significant absorption shift to the whole visible light region is observed with FPt0.5–TiO_2 nanocomposites, which was enhanced by increasing the amount of Pt as a dopant in TiO_2 matrix. Fig. 4b displays the corresponding band gap energies of TiO_2, F–TiO_2, and FPt*x*–TiO_2 synthesized nanocomposites calcined at 400 °C in air. The pure TiO_2 and F–TiO_2 nanomaterials exhibit very close band gap of 3.24 and 3.21 eV, respectively. In fact, the crystallinity of pure TiO_2 shown in Fig. 1 indicated that the TiO_2 was a mixture of anatase (3.2 eV) phase and less percentage of brookite (3.4 eV) phase, which logically can lead to this band gap value (3.24 eV). Moreover, as mentioned earlier,[20] fluorine controlled the growth of anatase phase which decreased the band gap of TiO_2 from 3.24 to 3.21 eV. Furthermore, the incorporation of Pt as a dopant in the TiO_2 lattice did not lead to a significant narrowing of the band gap while exhibiting strong absorption in the visible region. The incorporation of Pt (3%) in the TiO_2 matrix shifted the band gap from 3.21 to 3.02 eV (Table 1). The highly efficient absorption in the visible and near infrared regions originated from the existing of such color centers in the TiO_2 lattice, due to Pt as dopants, rather than the narrowing of the band gap energy of TiO_2. Indeed, the sites that give rise to this efficient absorption might correspond to the reduced titanium (Ti^{3+}) defects and oxygen vacancies centers photogenerated on the surface of TiO_2 nanoparticles.[34]

3.4.2 Potential energies positions. Fig. 5 shows the conduction band and valence band potential positions of pure TiO_2, F–TiO_2 and FPt3–TiO_2 nanocomposites. Most of metal oxide semiconductors have valence band between 1 and 3 eV, below the H_2O oxidation potential and the conduction band edges are close to, or lower than, the H_2O reduction potential.[35]

The conduction band of the pure TiO_2 is more negative than that of TiO_2 based nanocomposites (FPt*x*–TiO_2) due to the

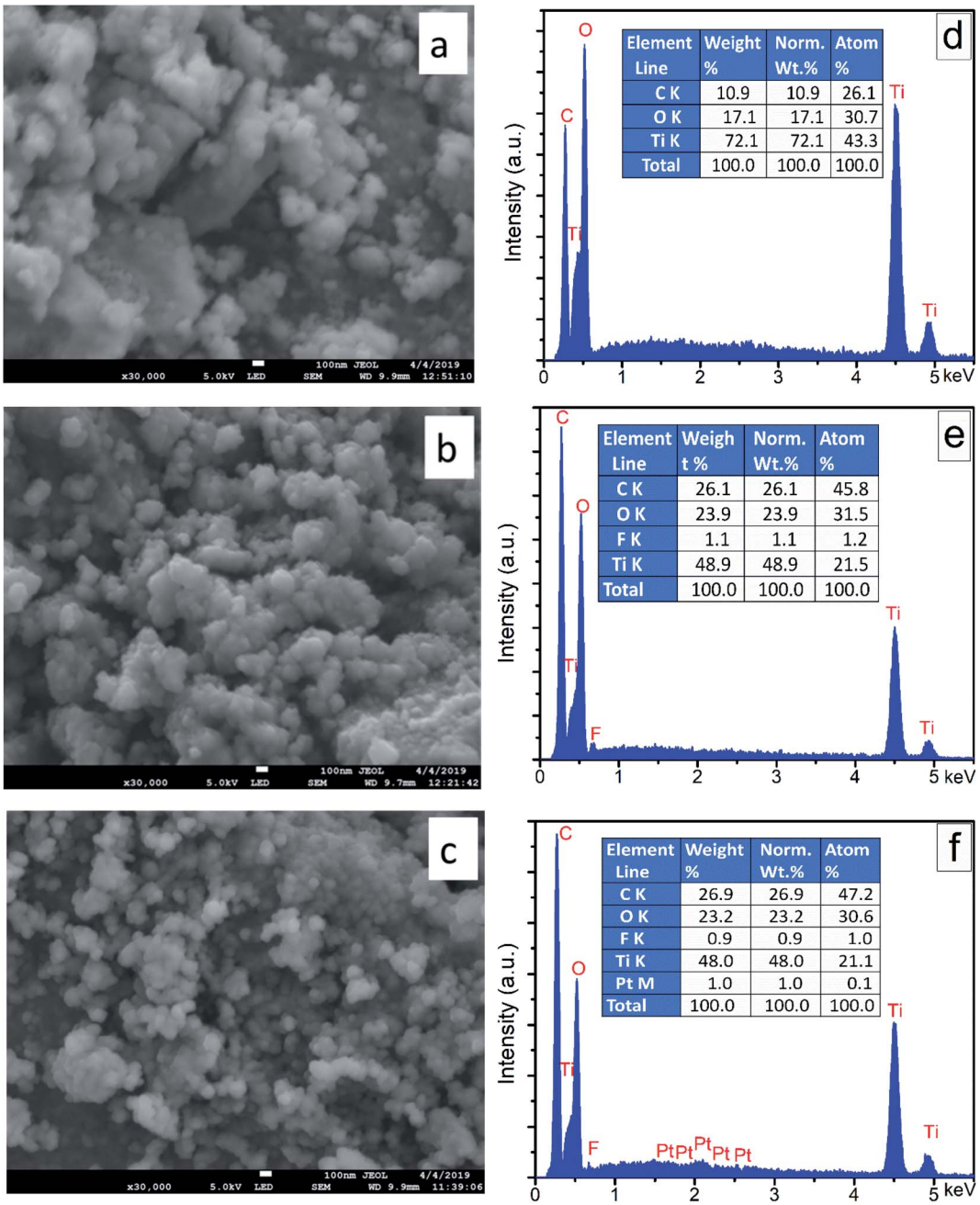

Fig. 2 (a)–(c) are HR-SEM images; (d), (e), and (f) are EDS of TiO_2, F–TiO_2, and FPt1–TiO_2 nanocomposites, respectively; calcined at 400 °C.

induction of new energy levels by co-doping TiO_2 with Pt and F; hence there is diffusion of electrons (e_{CB}^-) from the CB potential of TiO_2 to the new CB generated levels of TiO_2 based nanocomposites to react on the surface with the absorbed O_2 in order to generate superoxide anions ($O_2^{\bullet -}$) as super-oxidizing radicals for the degradation of SMX drugs. Meanwhile, the VB potential of TiO_2 is more positive than that of pure TiO_2, thus there is transfer of holes (h_{VB}^+) from the VB of TiO_2 to the new added energy level of TiO_2 based TiO_2 caused by the induction of F and Pt to react on the surface and then generate hydroxyl radicals ($^{\bullet}OH$) which also act for the destruction of SMX.[36,37] In addition, the incorporation of F and Pt into the TiO_2 lattice generate considerable defects, which tend to produce deep or low energy levels near the conduction band with typical Ti^{3+} states.[38] Table 1 presents the estimated band gap energies of TiO_2, F–TiO_2, and FPt*x*–TiO_2 nanocomposites prepared at 180 °C and calcined at 400 °C in air.

3.5 Photocatalytic degradation of SMX using solar simulator and direct solar light

The Fig. 6 shows the images of (SMX plus photocatalyst) solutions during the photocatalytic degradation process. Actually, the images demonstrate clearly the formation of a floating

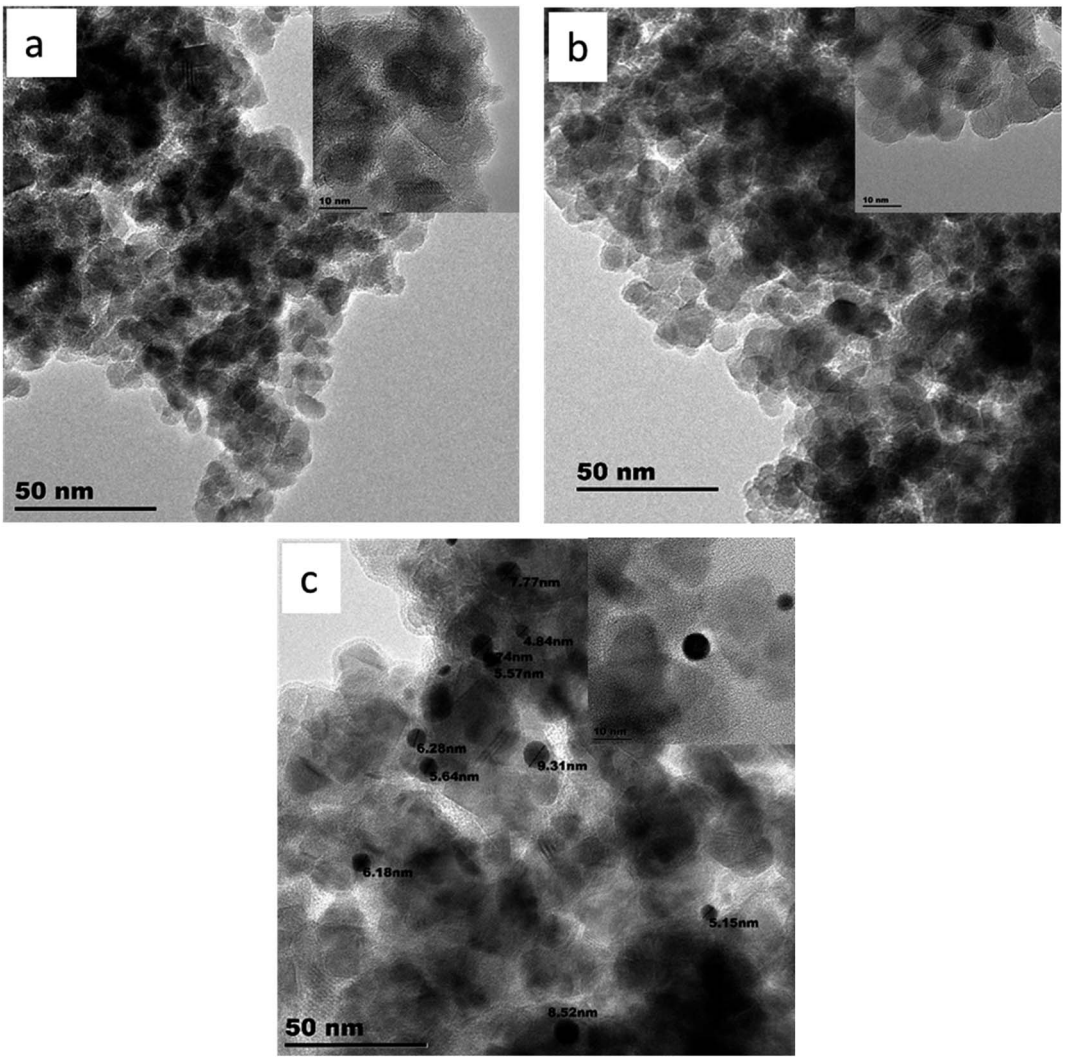

Fig. 3 TEM and HR-TEM images of (a) TiO_2, (b) F–TiO_2, and (c) FPt0.5–TiO_2 nanocomposites; calcined at 400 °C.

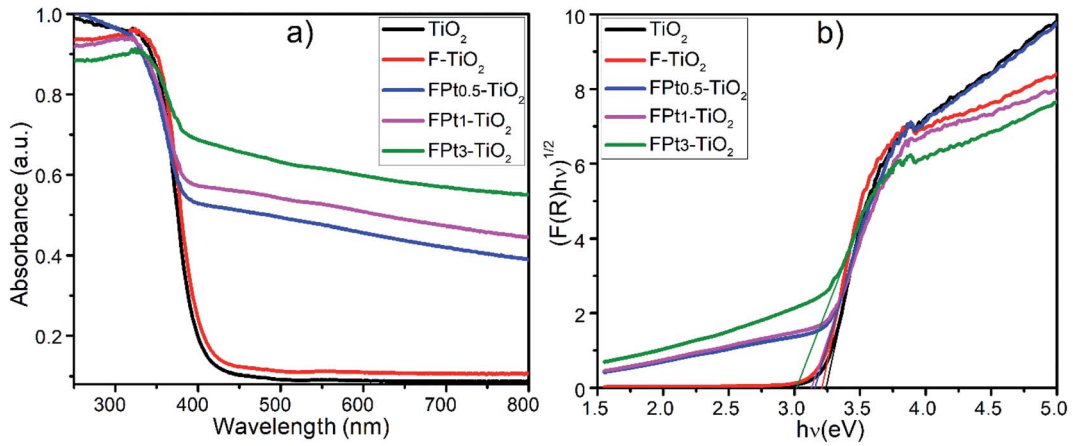

Fig. 4 (a) Absorbance and (b) optical band gap of TiO_2, F–TiO_2, and FPt*x*–TiO_2 nanocomposites, calcined at 400 °C. The band gap is achieved by substituting α by $F(R)$ in Tauc equation and extrapolation of the straight-line part of the Tauc plot ($(F(R)h\nu)^{1/2}$) against $h\nu$); thus, the intersection with the photon energy ($h\nu$) axes displays the band gap of the nanocomposites.

Table 1 Indirect Band gap, VB and CB energies of TiO_2, F–TiO_2 and FPt*x*–TiO_2 nanocomposites

Nanocomposite	Band gap (eV)	Valence band (eV)	Conduction band (eV)
TiO_2	3.24	2.93	−0.31
F–TiO_2	3.21	2.92	−0.29
FPt0.5–TiO_2	3.16	2.89	−0.27
FPt1–TiO_2	3.13	2.88	−0.25
FPt3–TiO_2	3.02	2.82	−0.2

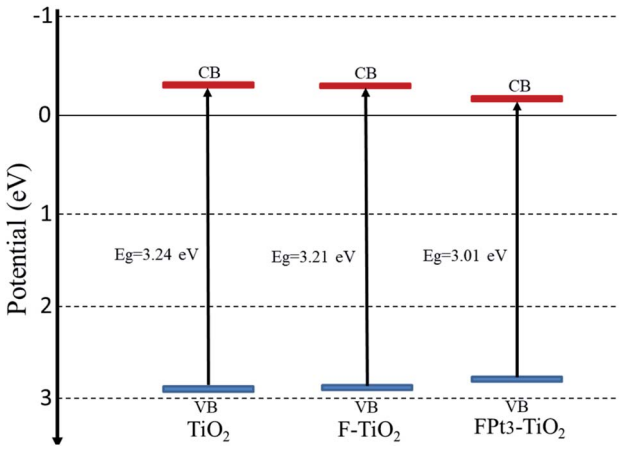

Fig. 5 Conduction band (red line) and valence band (blue line) positions of pure TiO_2, F–TiO_2 and FPt3–TiO_2 nanocomposites.

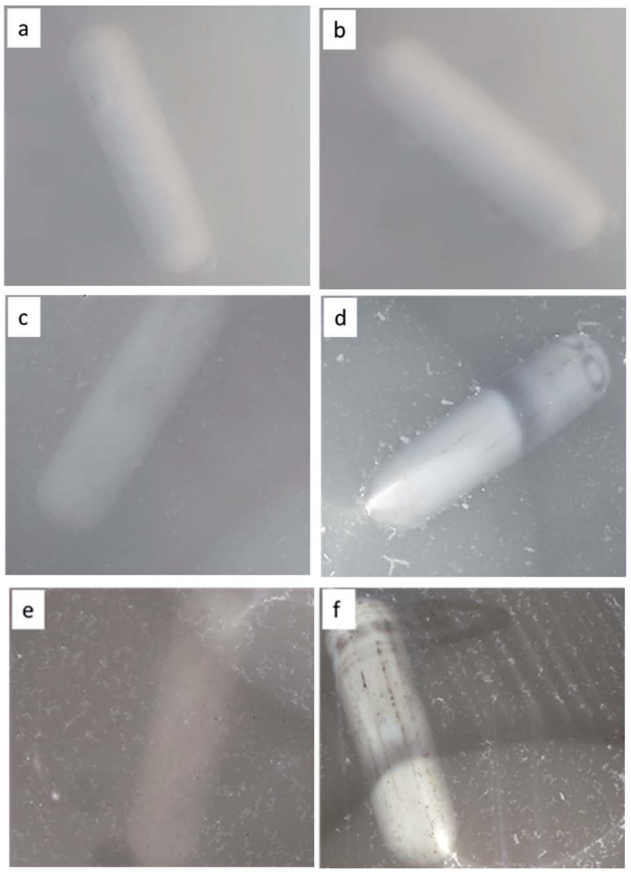

Fig. 6 (a), (c) and (e) images of (SMX + photocatalyst) solution after 30 min in dark; (b), (d) and (f) images of the treated solution after 120 min of photocatalytic degradation of SMX drug using TiO_2, F–TiO_2 and FPt3–TiO_2 nanocomposites, respectively.

product during the photocatalytic degradation of SMX. Fig. 6(a), (c) and (e) images were taken after 30 min in dark, while Fig. 6(b), (d) and (f) was taken after 120 min of photocatalytic degradation of SMX drug using TiO_2, F–TiO_2 and FPt3–TiO_2 nanocomposites under direct solar light, respectively. Fig. 6(a) and (b) images show a clean surface with no floatation of any product while other images show that the floatation of the generated polymer started after 30 min in dark (Fig. 6(c) and (d) images) and appears at high intensity after 120 min (Fig. 6(d) and (f)). Indeed, the floatation occurred only by including F^- in the TiO_2 lattice. The following images were taken during the photocatalytic degradation of SMX using direct sunlight, however it should be mentioned that there is floataion even with solar simulator of fluoropolymer.

3.5.1 Photocatalytic degradation using solar simulator. The photocatalytic degradation of 50 mL of SMX (20 mg L^{-1}) with 50 mg of FPt*x*–TiO_2 nanocomposites by using a Solar Simulator HAL-320 compart xenon light as energy light source is shown in Fig. 7; where the distance between the lamp of the solar simulator and the SMX solution is 26 cm. The power of light reaching to the surface of the solution (SMX plus photocatalyst) was measured by using digital lux meter; the light power variating between 14 630 and 18 360 LUXs. The temperature of the reaction medium was ranging between 31 and 33 °C. The degradation of SMX was slightly improved by increasing the amount of Pt from 0.5 to 3% in TiO_2 matrix as shown by Fig. 7(a)–(c). The photocatalytic degradation was incomplete at 360 minutes (min) after 30 min in dark even with FPt3–TiO_2. The wide absorbance gap shown by UV-Vis spectra (a)–(c) in Fig. 7, especially between 240 min and 360 min was due to the volume decrease of the treated solution. After sampling many times, the volume of the solution become less, thus, the degradation rate become fast. The light energy power supplied by the solar simulator was not sufficient to complete the degradation of SMX, hence, less than 60% of SMX degradation was achieved within 360 min while increasing the amount of Pt in TiO_2 matrix as shown in Fig. 7(d). To overcome this photocatalytic degradation weakness, the degradation of SMX has been moved under direct solar light irradiation.

Photocatalytic degradation rate of SMX has been previously studied by Chiang and Doong using 1g L^{-1} of pure TiO_2 and Cu deposited on TiO_2 surface but with less concentration of SMX (4 mg L^{-1}); where the photocatalytic degradation process initiated by irradiating the mixture with visible light irradiation after 30 min of stirring in dark (pH = 5.2). Indeed, the photocatalytic degradation rate of SMX, using pristine P25 TiO_2, was around 35% within 120 min which remains similar or slightly higher even by increasing the degradation time.[39] The reported results in the literature shows clearly that the unchanged TiO_2 has less effect on

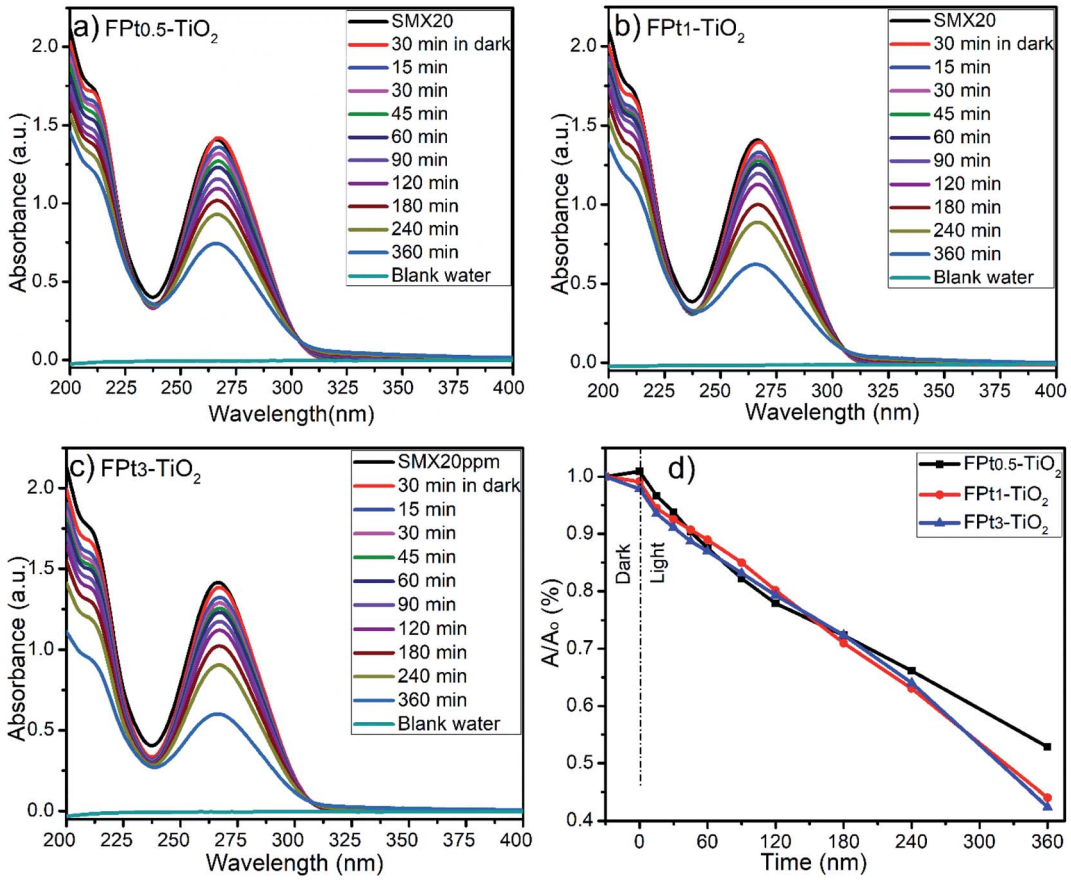

Fig. 7 UV-Vis spectra of SMX drug during the photocatalytic degradation process using (a) FPt0.5–TiO_2, (b) FPt1–TiO_2, and (c) FPt3–TiO_2 nanocomposites; (d) degradation efficiency under solar simulator irradiation.

the photocatalytic degradation of SMX which is in good agreement with the displayed results in this work. Ioannidou *et al.* reported a complete photocatalytic degradation of (1 mg L^{-1}) SMX, which is a very low concentration compared to that used in the present work (20 mg L^{-1}), within 120 min using 250 mg L^{-1} of P25 TiO_2 modified with tungsten under solar simulator irradiation.[40] Recently, Borowska *et al.* have investigated 50 mg L^{-1} of TiO_2 and TiO_2 modified with 1% of palladium and 1% of platinum for the degradation of 1 mg L^{-1} of SMX using solar light. Indeed, less than 5% of SMX was degraded using undoped TiO_2 within 30 min while almost complete degradation SMX within 10 min using palladium modified TiO_2 and around 90% of degradation was achieved within 30 min using platinum modified TiO_2,[41] which is matching with degradation rate in the present work. However, in the literature there is no reporting documents that shows the floatation of the degraded product except our earlier published work.[42]

In contrast with our results and the mentioned results above reported in the literature, Nasuhoglu *et al.* reported that the degradation rate of (12 mg L^{-1}) SMX diminishes as TiO_2 concentration increases using UV-C radiation ($\lambda_{max} = 254$ nm).[43]

3.5.2 Photocatalytic degradation using direct solar light. The UV-Vis absorption and degradation rate (A/A_0) of SMX drug during the photocatalytic degradation process using direct solar light irradiation is shown in Fig. 8. The degradation time of SMX was decreased from 360 min (after 30 min in dark) to 90 min with an increase of degradation rate from 57% (using solar simulator) to more than 93% (using direct solar light irradiation) (Fig. 7 and 8). The UV-Vis spectra show that the absorbance increased after 30 min in darkness. This was due to the sun heat which increase the temperature of the dark medium (adsorption–desorption equilibrium). This temperature which exceed 40 °C caused the evaporation of the solution which become more concentrated, thus, the absorbance of SMX after 30 min in dark increases. The UV-Vis spectra of SMX degradation using (a) TiO_2 and (b) F–TiO_2 nanomaterials showed almost same degradation rate (with small increase using F–TiO_2 which could be due the acidic medium caused by incorporating F^- ions into TiO_2 lattice) of less than 70% during 120 min. By using FPt0.5–TiO_2 and FPt1–TiO_2 nanocomposites, the photocatalytic degradation of SMX increased to about 84% within 120 min, while more than 93% of degradation was achieved within 90 min using the FPt3–TiO_2 nanocomposite as shown by UV-Vis spectra in Fig. 8(c), (d), and (e), respectively; as well the degradation rate (A/A_0) displayed by Fig. 8(f). The evaporation rate of SMX solution during the photocatalytic degradation process which making the solution more concentrated affect the degradation efficiency; thus, the degradation rate of SMX does not achieve 100%.

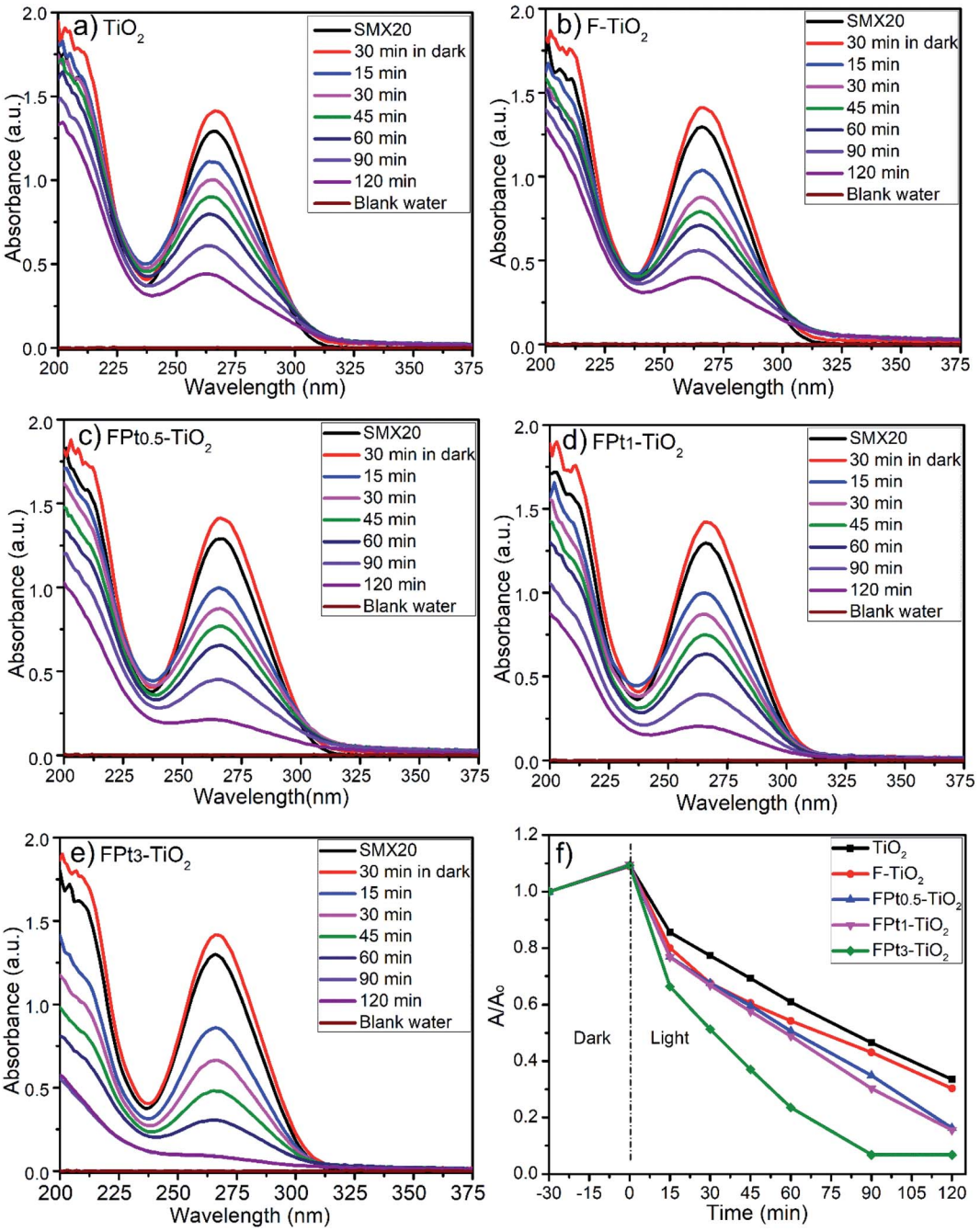

Fig. 8 UV-Vis spectra of SMX drug during the photocatalytic degradation process using (a) TiO_2 (b) F–TiO_2, (c) FPt0.5–TiO_2, (d)FPt1–TiO_2, (e) FPt3–TiO_2 nanocomposites; (f) degradation rate of SMX under direct solar light irradiation calculated from absorbance at λ_{max}.

Table 2 presents the photocatalytic degradation of SMX using solar simulator and direct solar light irradiations escorted with temperature of the reaction medium.

3.6 Kinetics of reaction

The kinetics of reaction occurred during the photocatalytic degradation of SMX using TiO_2 based nanocomposites can be described in such system by the Langmuir–Hinshelwood model:[44]

$$\frac{-dC}{dt} = \frac{K_r C}{1 + KC}$$

where C is the concentration of substrate, K_r is the reaction rate constant and K is the adsorption constant. For diluted solutions in which the substrate concentration is $<10^{-3}$ M, the value of $KC \ll 1$; thus, the equation can be simplified to pseudo-first order kinetic equation:[44,45]

$$-\ln\left(\frac{C_t}{C_0}\right) = kt$$

Table 2 Photocatalytic degradation of SMX using solar simulator and direct sunlight irradiations

	Degradation of SMX using solar simulator				Degradation of SMX using direct sunlight			
			T (°C)				T (°C)	
Nanocomposite	Degradation (%)	Time (min)	Dark	Light	Degradation (%)	Time (min)	Dark	Light
TiO_2	—	—	—	—	66.5	120	42	36–38
F–TiO_2	—	—	—	—	69.7	120	41	34–36
FPt0.5–TiO_2	47.3	360	33	28	83.8	120	42	35–37
FPt1–TiO_2	56	360	33	28	84.5	120	41	34–35
FPt3–TiO_2	57.6	360	33	28	93.2	90	41	33–34
					93.3	120	41	33–34

where C_0 and C_t are the initial concentration and concentration at time t, respectively. k is the reaction rate constant.

In order to study the kinetics of photocatalytic degradation of SMX using TiO_2 based nanocomposites, experiments were conducted under both solar simulator and direct sunlight irradiations. Meanwhile, calibration curve with $R^2 = 0.99651$ was investigated to determine the concentration for each specimen during the photocatalytic degradation process. Fig. 9(a)–(c) shows the calibration curve, kinetics of reaction using solar simulator and kinetics of reaction under direct sunlight irradiation, respectively. The photocatalytic degradation of SMX using F and Pt co-doped TiO_2 under both solar simulator and direct sunlight irradiations find to be commonly explained by the first-order kinetics as shown in Fig. 9(b) and (c), respectively. The photocatalytic degradation rate of SMX was fast using direct sunlight irradiation with respect to solar simulator irradiation which can be explained by the low intensity of solar simulator irradiation and wide wavelength range absorbed by TiO_2 based nanocomposites.

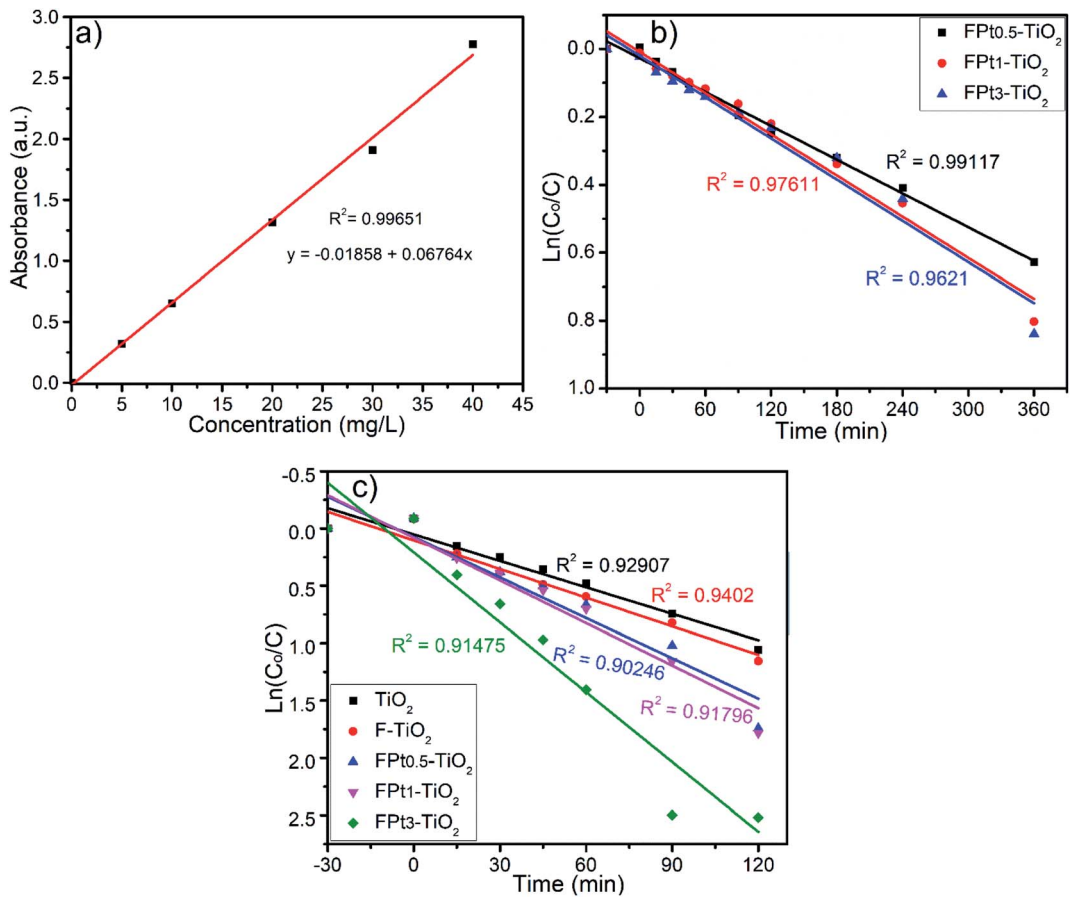

Fig. 9 (a) Calibration curve of SMX, (b) and (c) pseudo first-order kinetics using solar simulator and direct sunlight as source of light, respectively, for photocatalytic degradation of SMX using TiO_2, F–TiO_2 and FPtx–TiO_2 nanocomposites.

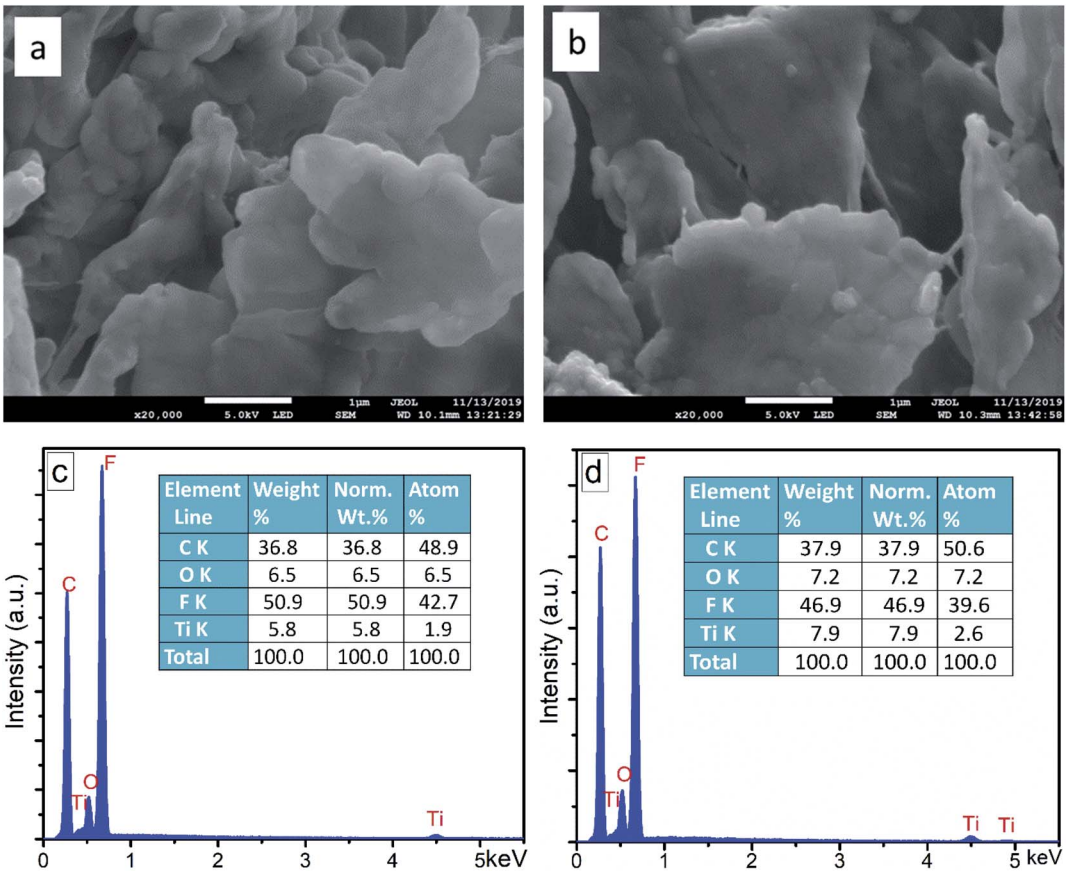

Fig. 10 SEM images and EDS analysis of the floated polymer after photocatalytic degradation of SMX drug using (a) and (c) F–TiO_2 and (b) and (d) FPt3–TiO_2, respectively.

3.7 SEM images and EDS analysis of the floated polymer after degradation of SMX

The external morphology and elemental composition of the floated product, *i.e.* F–TiO_2 and FPt3–TiO_2 photocatalysts after the degradation of SMX are shown by SEM images and EDS analysis (Fig. 10). The SEM images and EDS analysis of the floated product obtained after the photocatalytic degradation of SMX drug using F–TiO_2 and FPt3–TiO_2 nanocomposites, show similar morphology and same elemental composition. The morphology of the floated polymer displayed by (a) and (b) SEM is flat and with irregular shape. Meanwhile, the EDS analysis showed in Fig. 10(c) and (d) a very intense peak of fluorine with

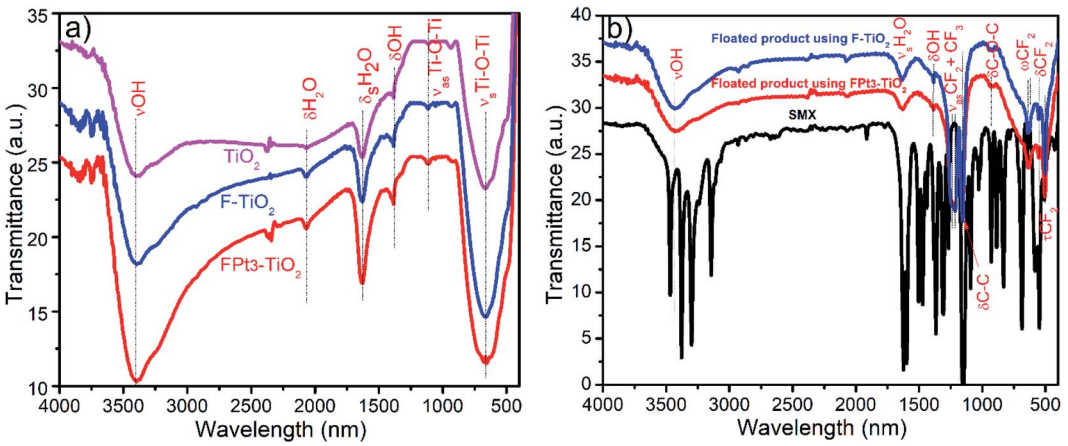

Fig. 11 FTIR of (a) synthesized photocatalysts used for photocatalytic degradation of SMX drug and (b) floated products collected after the photocatalytic degradation of SMX.

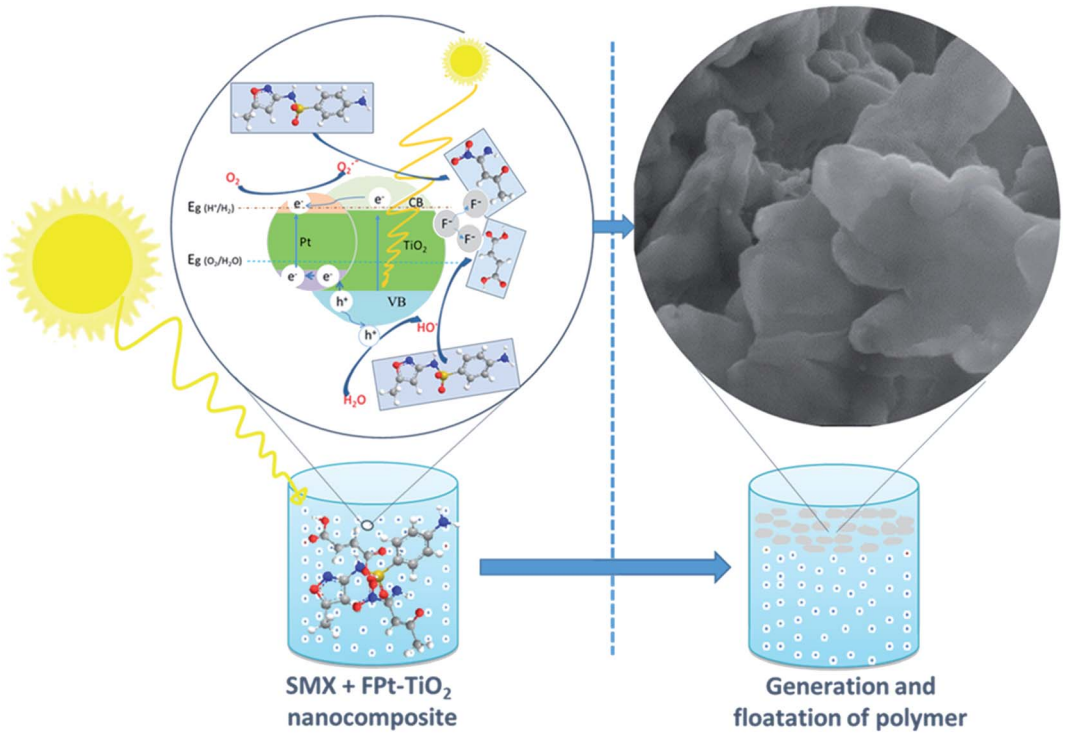

Fig. 12 Photocatalytic degradation pathways of SMX.

more than 46.9% of the elemental composition of the floated polymer as indicated in the elemental composition tables. This can only predict that the floated polymer is a metal-fluoropolymer. The absence of Pt in the elemental composition of the metal-fluoropolymer might be due to it low percentage or due to its non-contribution on the photogeneration of the floated polymer during the photocatalytic degradation of SMX drug.

3.8 Fourier-transform infrared (FT-IR) spectroscopy analysis

The FT-IR spectra of TiO_2, F–TiO_2, FPt3–TiO_2 nanocomposites, sulfamethoxazole drug and the floated product after the photocatalytic degradation of sulfamethoxazole drug using F–TiO_2 and FPt3–TiO_2 nanocomposites are given in Fig. 11. The spectra shown in Fig. 11(a) are characteristically similar of absorption peaks of TiO_2. Typically, the FT-IR spectra of TiO_2, F–TiO_2 and FPt3–TiO_2 nanocomposites (Fig. 11(a)) show a broad absorption band in the region of 3000–3642 cm^{-1} (with maximum at 3400 cm^{-1}) and 1635 cm^{-1} assigned to the stretching vibrations (νOH) and symmetric bending vibrations (δ_sOH) of absorbed water on the surface of the photocatalyst, respectively. Moreover, the peaks at 2068 and 1387 cm^{-1} were assigned to the bending mode of coordinated water (H–O–H) and O–H, respectively. The strong absorption peak in the region of 432–892 cm^{-1} with a maximum absorption at 665 cm^{-1} is attributed to the symmetric stretching vibrations of the Ti–O (ν_sTi–O).[46] The small peak at 1112 cm^{-1} was assigned to the asymmetric stretching vibrations of the Ti–O (ν_{as}Ti–O).[47]

On the other hand, the FT-IR spectra of SMX drug and floated product after degradation of SMX using F–TiO_2 and FPt3–TiO_2 photocatalyst are shown in Fig. 11(b); hence, there are no similarity between the floated product and SMX drug. It should be mentioned that all the bands appeared in the spectra of the photocatalyst are present in the FT-IR spectra of the floated product except ν_sTi–O and ν_{as}Ti–O. Bands located on the floated product spectra at 1216 and 1155 cm^{-1} assigned to the (CF_3 and CF_2) asymmetric and (CF_2) symmetric stretching vibrations, respectively.[48,49] The small band at 929 cm^{-1} was assigned to the bending vibration of C–O–C group.[50] The doublets at 640 and 625 cm^{-1} are matched to the CF_2 wagging vibrations.[48] Additionally, the two bands on the floated product spectrum, using F–TiO_2 and FPt3–TiO_2 photocatalysts, located at 556 and 506 cm^{-1} reflect the CF_2 bending and twisting vibrations, respectively.[51,52] The FT-IR analysis confirm that the generated product floated on the surface of the treated solution is due to the presence of fluoride irons (F^-) which further react with the degraded products to form a metal-fluoropolymer.[42]

3.9 Possible photocatalytic degradation pathways of SMX

Fig. 12 illustrates the possible photocatalytic degradation of SMX followed by fluorination of the degraded products and then floatation of the formed polymer using the FPt*x*–TiO_2 nanocomposites prepared *via* a one-step microwave-assisted hydrothermal method. The photocatalytic degradation process starts in the dark to assure the equilibrium absorption–desorption of SMX on the surface of FPt–TiO_2 nanocomposites. This is where the superoxide anions ($O_2^{\bullet-}$) and hydroxyl radicals ($^{\bullet}OH$) initially formed, after the exposure of FPt–TiO_2 surface to the light, due to the oxidation of O_2 and H_2O existing on the surface of the prepared photocatalyst (FPt–TiO_2).[53] These

superoxide anions and hydroxyl radicals exhibiting the power of oxidation destruction degrade SMX to smaller fragments which is fluorinated by fluoride ions and act to form a polymer floating on the surface of the treated solution as demonstrated in Fig. 12.[42]

The presence of fluorine induces the replacement of ≡Ti–OH groups located on the surface of TiO_2 nanoparticles by ≡Ti–F groups, thus generate free hydroxyl radicals (˙OH) with larger redox potential than that of ˙OH radicals adsorbed on surface TiO_2.[54,55] The fluoride ions, therefore, present a positive effect on the photocatalytic activity of TiO_2 when the reaction happening on the surface of the nanoparticles requires the intervention of the ˙OH radicals, but in the main time has a negative effect when the reaction proceeds through the photogenerated holes.[55,56] Hence, the presence fluorine on the surface of TiO_2 can only acts using free ˙OH radicals formed and dispersed in the reaction solution for the degradation of SMX drugs, instead of the photogenerated ˙OH radicals on the surface of TiO_2. Meanwhile, SMX can be destructed directly on the surface of platinum as a result of electron escape, as well as indirectly by photogenerated oxidizing radicals: $O_2^{\cdot -}$ from excited electrons on the conduction band ($e_{CB}-$) and ˙OH from the holes leaving after excitation of electrons on the valence band (h_{VB}^+).[36] On the other hand, the fluoride radical ions photogenerated on the surface of TiO_2 acts for the fluorination of TiO_2 the degraded products and finally floatation as fluoropolymer.[42]

4. Conclusions

TiO_2, F–TiO_2 and FPt*x*–TiO_2 nanocomposites were successfully synthesized *via* a facile hydrothermal-assisted microwave process and investigated for the photocatalytic degradation of SMX drug. The prepared photocatalysts possessed multiple roles on the photocatalytic removal of SMX such as photocatalytic degradation, photo-generation of a new product (referred to as metal-fluoropolymer), and then floatation of resulting product. This unique kind of photocatalysts will attract a lot of interest in the future as it provides a facile route towards micropollutants degradation and removal. The incorporation of fluoride ions in the TiO_2 lattice serves to (i) control the growth of anatase phase, which is the most suitable photocatalytic active phase in TiO_2, and (ii) enhance the fluorination process of the degraded products. On the other hand, platinum, known as an electrochemical catalyst, was used to add new energy levels between the valence band and conductive band of TiO_2 in order to narrow the band gap of TiO_2 thereby broadening the photocatalytic absorption to the visible and near infrared regions. The photocatalytic performance of the synthesized photocatalysts was studied using SMX drug under both solar simulator and direct sunlight irradiations. The photocatalytic performance increased by using direct solar irradiations, hence, the degradation time was reduced from 360 min after 30 min in the dark (with a degradation efficiency *ca* 57% using solar simulator) to 90 min after 30 min in dark (with a degradation efficiency > 93% using direct sunlight irradiation).

Conflicts of interest

The authors announce that there are no conflicts to declare.

Acknowledgements

This work was supported by the University of South Africa (Nanotechnology and Water Sustainability Research Unit), the National Research Foundation (NRF), and the Water Research Commission (WRC).

References

1 M. Patel, R. Kumar, K. Kishor, T. Mlsna, C. U. Pittman and D. Mohan, *Chem. Rev.*, 2019, **119**, 3510–3673.
2 S. A. Kraemer, A. Ramachandran and G. G. Perron, *Microorganisms*, 2019, **7**, 180.
3 V. Calisto, C. P. Silva, V. I. Esteves, D. L. D. Lima, C. Oliveira and M. Otero, *Sci. Total Environ.*, 2018, **648**, 1403–1410.
4 L. Yang, L. Jiang, X. Cao, M. Inyang, Y. Yao, B. Gao, H. Chen, A. R. Zimmerman, H. Li and Y. Xue, *J. Hazard. Mater.*, 2012, **209–210**, 408–413.
5 W. Ouyang, E. Kuna, A. Yepez, A. Balu, A. Romero, J. Colmenares and R. Luque, *Nanomaterials*, 2016, **6**, 93.
6 M. V. Dozzi, C. D'Andrea, B. Ohtani, G. Valentini and E. Selli, *J. Phys. Chem. C*, 2013, **117**, 25586–25595.
7 M. Kapilashrami, Y. Zhang, Y.-S. Liu, A. Hagfeldt and J. Guo, *Chem. Rev.*, 2014, **114**, 9662–9707.
8 K. H. Leong, H. Y. Chu, S. Ibrahim and P. Saravanan, *Beilstein J. Nanotechnol.*, 2015, **6**, 428–437.
9 X. Qin, Z. Zheng, Y. Dai, X. Zhang, M.-H. Whangbo and B. Huang, *J. Mater. Chem.*, 2011, **21**, 9079–9087.
10 X. Chen and S. S. Mao, *Chem. Rev.*, 2007, **107**, 2891–2959.
11 N. Roy, K. T. Leung and D. Pradhan, *J. Phys. Chem. C*, 2015, **119**, 19117–19125.
12 J. Gomes, R. Costa, A. Lopes, R. Quinta-Ferreira, K. Bednarczyk, M. Gmurek, M. Quinta-Ferreira, A. Zaleska-Medynska, M. Stelmachowski and R. Martins, *ChemEngineering*, 2018, **2**, 1–14.
13 X. Xiong and Y. Xu, *J. Phys. Chem. C*, 2016, **120**, 3906–3912.
14 Y. Hu, X. Song, S. Jiang and C. Wei, *Chem. Eng. J.*, 2015, **274**, 102–112.
15 F. Zhang, J. Chen, X. Zhang, W. Gao, R. Jin, N. Guan and Y. Li, *Langmuir*, 2004, **20**, 9329–9334.
16 R. Jaiswal, N. Patel, A. Dashora, R. Fernandes, M. Yadav, R. Edla, R. S. Varma, D. C. Kothari, B. L. Ahuja and A. Miotello, *Appl. Catal., B*, 2016, **183**, 242–253.
17 R. Jaiswal, J. Bharambe, N. Patel, A. Dashora, D. C. Kothari and A. Miotello, *Appl. Catal., B*, 2015, **168–169**, 333–341.
18 H. Sun, S. Wang, H. M. Ang, M. O. Tadé and Q. Li, *Chem. Eng. J.*, 2010, **162**, 437–447.
19 A. M. Czoska, S. Livraghi, M. Chiesa, E. Giamello, S. Agnoli, G. Granozzi, E. Finazzi, C. Di Valentiny and G. Pacchioni, *J. Phys. Chem. C*, 2008, **112**, 8951–8956.
20 T. Butburee, P. Kotchasarn, P. Hirunsit, Z. Sun, Q. Tang, P. Khemthong, W. Sangkhun, W. Thongsuwan,

P. Kumnorkaew, H. Wang and K. Faungnawakij, *J. Mater. Chem. A*, 2019, **7**, 8156–8166.
21 J. C. Yu, J. Yu, W. Ho, Z. Jiang and L. Zhang, *Chem. Mater.*, 2002, **14**, 3808–3816.
22 D. Li, H. Haneda, S. Hishita, N. Ohashi and N. K. Labhsetwar, *J. Fluorine Chem.*, 2005, **126**, 69–77.
23 Z. Zhang, O. Bondarchuk, B. D. Kay, J. M. White and Z. Dohnálek, *J. Phys. Chem. C*, 2007, **111**, 3021–3027.
24 P. Ganguly, S. Mathew, L. Clarizia, S. Kumar R, A. Akande, S. Hinder, A. Breen and S. C. Pillai, *Appl. Catal., B*, 2019, **253**, 401–418.
25 M. Jahdi, S. B. Mishra, E. N. Nxumalo, S. D. Mhlanga and A. K. Mishra, *Opt. Mater.*, 2020, **104**, 109844.
26 M. Mousavi, A. Habibi-Yangjeh and M. Abitorabi, *J. Colloid Interface Sci.*, 2016, **480**, 218–231.
27 R. S. Mulliken, *J. Chem. Phys.*, 1934, **2**, 782–793.
28 E. M. Samsudin, S. B. A. Hamid, J. C. Juan, W. J. Basirun, A. E. Kandjani and S. K. Bhargava, *Appl. Surf. Sci.*, 2016, **365**, 57–68.
29 M. D. Dramićanin, Z. Antić, S. Ćulubrk, S. P. Ahrenkiel and J. M. Nedeljković, *Nanotechnology*, 2014, **25**, 485501.
30 J. G. Li, C. Tang, D. Li, H. Haneda and T. Ishigaki, *J. Am. Ceram. Soc.*, 2004, **87**, 1358–1361.
31 W. Kang, C. S. Spanjers, R. M. Rioux and J. D. Hoefelmeyer, *J. Mater. Chem. A*, 2013, **1**, 7717–7728.
32 K. Huang, K. Sasaki, R. R. Adzic and Y. Xing, *J. Mater. Chem.*, 2012, **22**, 16824–16832.
33 Z. Yao, M. Zhu, F. Jiang, Y. Du, C. Wang and P. Yang, *J. Mater. Chem.*, 2012, **22**, 13707–13713.
34 J. L. Gole, J. D. Stout, C. Burda, Y. Lou and X. Chen, *J. Phys. Chem. B*, 2004, **108**, 1230–1240.
35 X. Yong and M. A. A. Schoonen, *Am. Mineral.*, 2000, **85**, 543–556.
36 D. Benz, K. M. Felter, J. Köser, J. Thöming, G. Mul, F. C. Grozema, H. T. Hintzen, M. T. Kreutzer and J. R. van Ommen, *J. Phys. Chem. C*, 2020, **124**, 8269–8278.
37 Q. Yuan, L. Chen, M. Xiong, J. He, S. L. Luo, C. T. Au and S. F. Yin, *Chem. Eng. J.*, 2014, **255**, 394–402.
38 X. Chen, L. Liu, P. Y. Yu and S. S. Mao, *Science*, 2011, **331**, 746.
39 L. F. Chiang and R. A. Doong, *Sep. Purif. Technol.*, 2015, **156**, 1003–1010.
40 E. Ioannidou, Z. Frontistis, M. Antonopoulou, D. Venieri, I. Konstantinou, D. I. Kondarides and D. Mantzavinos, *Chem. Eng. J.*, 2017, **318**, 143–152.
41 E. Borowska, J. F. Gomes, R. C. Martins, R. M. Quinta-Ferreira, H. Horn and M. Gmurek, *Catalysts*, 2019, **9**, 500.
42 M. Jahdi, S. B. Mishra, E. N. Nxumalo, S. D. Mhlanga and A. K. Mishra, *Appl. Catal., B*, 2020, **267**, 118716.
43 D. Nasuhoglu, V. Yargeau and D. Berk, *J. Hazard. Mater.*, 2011, **186**, 67–75.
44 M. Długosz, P. Zmudzki, A. Kwiecień, K. Szczubiałka, J. Krzek and M. Nowakowska, *J. Hazard. Mater.*, 2015, **298**, 146–153.
45 A. Mirzaei, L. Yerushalmi, Z. Chen, F. Haghighat and J. Guo, *Water Res.*, 2018, **132**, 241–251.
46 H. Khan, M. G. Rigamonti, G. S. Patience and D. C. Boffito, *Appl. Catal., B*, 2018, **226**, 311–323.
47 G. Devanand Venkatasubbu, S. Ramasamy, V. Ramakrishnan and J. Kumar, *Adv. Powder Technol.*, 2013, **24**, 947–954.
48 T. Hwang, V. Palmre, J. Nam, D. C. Lee and K. J. Kim, *Smart Mater. Struct.*, 2015, **24**, 105011.
49 C. Guo, M. Xu, S. Xu and L. Wang, *Nanoscale*, 2017, **9**, 7163–7168.
50 M. Zhao, Y. Yu, Z. Han and H. Li, *Polymers*, 2017, **9**, 606.
51 L. N. Ignatieva, G. A. Zverev, N. A. Adamenko, A. V. Kazurov and A. Y. Ustinov, *J. Fluorine Chem.*, 2019, **217**, 58–62.
52 J. Mihály, S. Sterkel, H. M. Ortner, L. Kocsis, L. Hajba, É. Furdyga and J. Minka, *Croat. Chem. Acta*, 2006, **79**, 497–501.
53 M. V. Sofianou, V. Psycharis, N. Boukos, T. Vaimakis, J. Yu, R. Dillert, D. Bahnemann and C. Trapalis, *Appl. Catal., B*, 2013, **142–143**, 761–768.
54 J. Yu, W. Wang, B. Cheng and B. L. Su, *J. Phys. Chem. C*, 2009, **113**, 6743–6750.
55 J. F. Montoya and P. Salvador, *Appl. Catal., B*, 2010, **94**, 97–107.
56 M. Bellardita, C. Garlisi, A. M. Venezia, G. Palmisano and L. Palmisano, *Catal. Sci. Technol.*, 2018, **8**, 1606–1620.